Hierarchically structured metal–organic framework/vertically-aligned carbon nanotubes hybrids for CO_2 capture†

Lei Ge, Li Wang, Victor Rudolph and Zhonghua Zhu[*]

A novel carbon/metal–organic framework composite was synthesized by confined growth of HKUST-1 in the interspace of the vertically-aligned carbon nanotube (VACNT) arrays. The grown HKUST-1 crystals are much smaller than the HKUST-1 crystals produced without the confinement growth. The derived HKUST-1/VACNT hybrids possess a hierarchical microporous–mesoporous structure. In comparison to the calculated hypothetical value assuming the physical mixture of the components, the synthesized HKUST-1/VACNT composites exhibit larger surface area and porosity, higher CO_2 adsorption amount, and better CO_2/N_2 selectivity, which indicate the positive synergistic effect between HKUST-1 and VACNT. Besides the superior adsorption properties of hybrids, they are easier to handle than powder adsorbent for gas storage/separation.

Introduction

Metal–organic frameworks (MOFs) or porous coordination polymers (PCPs) are a new class of porous crystalline materials, which have attracted a great deal of attention over the past decade.[1] A lot of these fascinating crystalline hybrid materials have been synthesized and studied worldwide; their promising applications have been involved in many different areas, such as adsorption,[2,3] catalysis,[4] drug delivery,[5] chemical sensor[6] and separation membranes.[7,8]

Though some achievements have been made, the potential applications of MOFs have not yet been realized in industry.[9] One of the main reasons to hold back the industrial application of MOFs is their stability; they tend to experience a dramatic drop in their surface area and sorption capacity when exposed to moisture. In addition, the narrow micropores of MOFs restrict the fast gas diffusion inside the pores, limiting their industrial applications in adsorption, catalysis and gas separations. A key technology to realise the extensive applications of powdered materials is to develop hierarchically structured bulk materials to overcome the above problems.[10] By tailoring the ratio of macropores, mesopores and micropores of the bulk materials, low pressure drop and high mass transfer can be obtained simultaneously. Moreover, the bulk structure enables

the fast heat transfer and minimal mass loss during the application. Therefore, hierarchically structured bulk materials are ideal for process intensification. Some previous work has shown that MOFs with hierarchically pores can be obtained by applying longer organic spacers or surfactants; yet the process is difficult to handle, and the small change in reactants or solvents may result in nonporous or poorly crystalline structure in MOFs.[11,12]

The fabrication of MOFs based composites can be one promising route to achieve the hierarchical pore structure. Research on MOFs based composites has mainly focused on growing MOFs on siliceous materials or incorporating carbon materials into MOFs.[13–16] Yang *et al.*[14] prepared carbon nanotube (CNT)/MOF-5 hybrid composite and found that the surface area and the hydrogen storage capacity were significantly improved compared to pure MOF-5. Xiang *et al.*[17] synthesized the CNT/[Cu3(BTC)2] hybrid *via* CNT incorporation. The CO_2 and CH_4 uptakes on this composite increased dramatically compared to the unmodified MOFs. Further improvement can be achieved by doping the CNT-modified MOFs with certain amount of Li.[18] Prasanth *et al.*[19] incorporated single walled carbon nanotubes into MIL-101. The composite shows increased hydrogen adsorption with tunable pore size and pore volume. The increment of CO_2 adsorption was also found in multi-walled CNTs/MIL-101 composite.[20] Bandosz group has investigated serials of MOF and graphite oxide (GO) composites.[13,21–25] The enhanced pore volumes of composite was observed, which can be attributed to the reaction of organic linker with the functional groups of GO. Synergistic effects on porosity and chemistry properties can lead to significant improvements on adsorption capacity and selectivity. Silica materials were also incorporated with MOFs,

The University of Queensland, School of Chemical Engineering, Brisbane 4072, Australia. E-mail: z.zhu@uq.edu.au; Fax: +61 7 3365 4199; Tel: +61 7 33653528

† Electronic supplementary information (ESI) available: Experimental details, digital images, TGA, N_2-adsorption of HKUST-1 and HKUST-1/VACNT composite, CO_2 and N_2 adsorption isotherms of HKUST-1, high pressure CO_2 adsorption, Langmuir–Freundlich isotherm fit for adsorption, element analysis results of HKUST-1/VACNT composite. See DOI: 10.1039/c3ra44250k

which displayed stable structure. The HKUST-1/MCM-41 composites showed high stability and high ammonia removal capability.[15] To summary, various MOFs based composites have been successfully synthesized with improved specific surface area and gas sorption capacity. However, by incorporating carbon or silica materials into MOFs, the derived composites are still in powder shape.

The conventional techniques using fine powder particles in gas adsorption and chemical reactions suffer from a number of drawbacks during operation, such as large pressure drop, poor controllability on mass transfer, low thermal conductivity, severe material loss due to carryover and less flexibility for pore network adjustment. As to the finer the particles, the more the gates for the gas to come in/out, and the more difficulty for the pore network to be adjusted. In addition, it will be much harder for fine particles to realize the gas storage at low pressure. Therefore, the design of hierarchical bulk structured materials can be an effective way to solve these issues in adsorption.

In this study, the hierarchically structured MOFs/vertically-aligned carbon nanotube (VACNT) bulk composites were fabricated by confinement growth of MOFs into VACNT arrays. The VACNT will enhance the dispersive interactions between MOFs and CNTs, therefore, the MOFs component will contribute to the expansion of the micropore space which favour the storage of the adsorbate. Another benefit provided by VACNT is the superior thermal conductivity, which can also greatly improve the thermal conductivity of the composite for the real adsorption application. HKUST-1 is selected in this study due to its high thermal and structural stability as well as its excellent CO_2 adsorption performance.

Experimental details

Aligned carbon nanotube growth

The growth of carbon nanotubes was conducted by chemical vapour decomposition (CVD) of a gas mixture of catalyst source (ferrocene) and carbon source (camphor) on quartz substrate, using the pyrolysis apparatus as outlined in an earlier study.[26,27] A two-stage furnace system fitted with a quartz tube (inner diameter: 47 mm, length: 1.1 m) was used as the reactor. The mixture of the ferrocene (Sigma-Aldrich, 99% pure) and camphor (Sigma-Aldrich, 99.5% pure) with a camphor–ferrocene weight ratio adjusted at 10 was put into a quartz boat and placed inside the first part of quartz tube. The commercial quartz substrates, which had been cleaned with acetone, were located in the second part of the quartz tube at measured distances from the quartz boat. Before the CVD process, Ar gas (Coregas, 99.999%) was initially flowed through the tube reactor to remove the residue air as the second furnace was heated up to the CVD temperature, 900 °C. After the second furnace attained the CVD temperature, the camphor–ferrocene mixture was heated up in the first furnace at a heating rate of 15 °C min^{-1} until the temperature reached ~155 °C. Argon gas was then flowed through the quartz tube at a flow rate of 1.1 l min^{-1} to blow the camphor–ferrocene vapour into the second furnace. The concentration of water vapour in the gas flow was controlled by applying an argon stream passing through a water

saturator at a flow rate of 5 ml min^{-1} with the corresponding water concentration in the gas flow of around 80 ppm. The thermal CVD was conducted at 900 °C for 30 min, and after that, the reactor was cooled to room temperature under pure Ar atmosphere with the moist argon switched off. A deposit of carbon was found on the substrates and tube inner surfaces.

Synthesis of HKUST-1 and HKUST-1/VACNT composite

HKUST-1 and HKUST-1/VACNT composite was prepared *via* procedures reported in previous works.[28] About 1.0 g benzene-1,3,5-tricarboxylic acid (Sigma-Aldrich, 99.5% pure) was dissolved in 30 ml of a 1 : 1 mixture of ethanol–dimethylformamide (DMF, analytical grade, Sigma-Aldrich). In another beaker, about 2.077 g $Cu(NO_3)_2 \cdot 3H_2O$ (Sigma-Aldrich, 99.5% pure) were dissolved in 15 ml water. Two solutions were then mixed and stirred for 10 min before transferring into a Teflon-lined stainless steel autoclave, and then the hydrothermal reactions were conducted at 100 °C for 7 h.

The VACNT arrays on a quartz substrate of 5 cm × 2.5 cm were applied for the confinement growth of HKUST-1. Before the *in situ* growth of HKUST-1 on VACNTs, the as-obtained VACNT arrays were treated in 30% hydrogen peroxide solution at 100 °C for 3 h followed by H_2O wash and drying. After that, the VACNT forests were further treated with 30 vol.% APTES/NMP solution at 100 °C for 3 h. The treated VACNTs were washed with water for several time and dried in vacuum. The untreated VACNT will be specifically mentioned to distinguish the treated VACNT in this work. For synthesizing HKUST-1/VACNT hybrid, the as-obtained VACNT or APTES-treated VACNT arrays were put into the autoclave and immersed into the HKUST-1 precursor solution horizontally for the hydrothermal reaction. The reaction conditions were the same to the synthesis of HKUST-1 as mentioned above. After cooling, the resulting HKUST-1 or HKUST-1/VACNT composite on the quartz substrate were washed by DMF twice, and immersed into ethanol solvents to remove the solvated DMF. After that, the samples were degassed at 80 °C in vacuum. The HKUST-1/VACNT carpets were carefully removed from the substrate and broken into pieces for later use.

Characterization

The X-ray diffraction spectra (XRD) of HKUST-1 crystals were obtained using a Bruker Advanced X-ray Diffractometer (40 kV, 30 mA) with Cu Kα ($\lambda = 0.15406$ nm) radiation at a scanning rate of 1° min^{-1} from 10° to 70°. Attenuated total reflection Fourier transform infrared spectra (ATR-FTIR) were obtained using a Nicolet 5700 ART spectrometer with an average of 64 scans in the range 400–3800 cm^{-1}. A JEOL JSM 6300 operated at 5 kV was used for scanning electron microscopy (SEM) and a JEOL 6610 coupling with an Oxford SDD energy dispersive X-ray spectrometer (EDS) was used for elemental analysis. Transmission electron microscopy (TEM) and high-resolution transmission electron microscopy (HRTEM) were performed on a JEOL JEM-2100 microscope, with accelerating voltages of 200 kV. The samples were dispersed by sonication in ethanol, then deposited on a holey carbon TEM grid and dried. Thermogravimetric analysis (TGA) was carried out from 50 to 800 °C at 5 °C min^{-1}

under air using a Perkin Elmer Instruments STA 6000 Thermogravimetric Analyzer.

N_2 physisorption isotherms of the samples were obtained using a Micromeritics TriStar II 3020 at -196 °C, after degassing the samples for 24 h at 150 °C. The corresponding specific surface areas were calculated by the Langmuir equation at relative pressure (P/P_0) between 0.005 and 0.05. After N_2 adsorption, the samples were degassed at 150 °C under a pressure of 10 mTorr until no further pressure drop was observed. The adsorption equilibrium of CO_2 and N_2 at 30 °C was then measured using the same instrument by immersing the sample tube in a temperature-controlled water bath. The variation in the sample temperature was minimal (<0.1 °C). Desorption isotherm of the CO_2 or N_2 adsorbed in the sample was obtained by gradually decreasing the system pressure to 10 mTorr. High-pressure sorption of CO_2 and N_2 was carried out at 35 °C in a BEL-BG instrument with a high-accuracy magnetic suspension balance (Rubotherm). About 0.2 g of HKUST-1/VACNT composite was degassed at 80 °C under vacuum for 2–4 h prior to high-pressure adsorption.

Results and discussion

Fig. 1 shows the XRD patterns of the HKUST-1 and HKUST-1/VACNT hybrids. The structure parameters obtained by Rietveld refinements are presented in Table S1 (ESI†). Based on the HKUST-1 structure data,[29,30] the observed pattern and the simulated pattern show high similarity, confirming the formation of pure crystalline HKUST-1. The confined growth of HKUST-1 into the interspaces of VACNT is also confirmed by the XRD pattern since the spectrum of HKUST-1/VACNT composite is similar to that of pure HKUST-1. In addition, there exists SiO_2 phase in HKUST-1/VACNTs, which can be assigned to the quartz substrate of VACNTs.

The digital images in Fig. S1 (ESI†) show the morphology of HKUST-1 particles, VACNT carpets and HKUST-1/VACNT bulk composite. Compared to the powder shape of HKUST-1, the HKUST-1/VACNT composite displays bulk shape by the confinement growth of HKUST-1 in VACNT arrays. Larger scale synthesis of HKUST-1/VACNT bulk composite can be easily achieved by the scale-up of the VACNT carpet synthesis and the HKUST-1 hydrothermal growth. Fig. 2 shows the microscopy morphology of VACNT arrays, the synthesized HKUST-1 crystals and HKUST-1/VACNT hybrid. In Fig. 2a, the VACNT arrays show
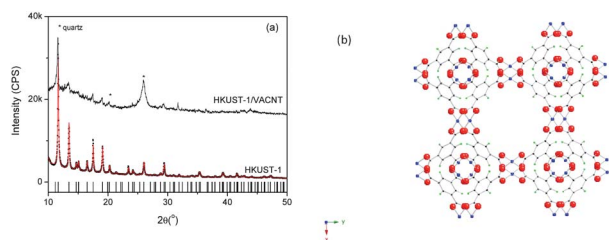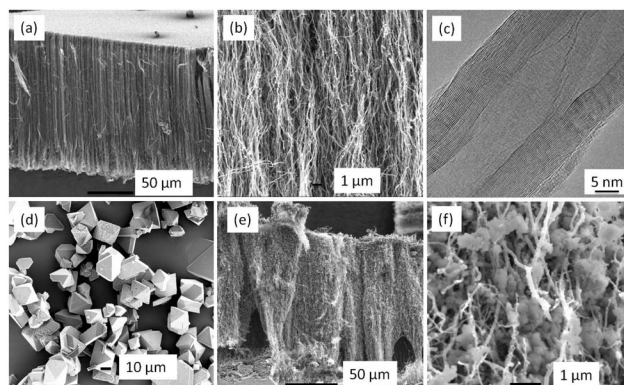
Fig. 2 SEM and TEM morphologies of as-synthesized VACNTs (a–c), HKUST-1 (d) and HKUST-1/VACNT hybrid (e and f).

high degree of vertical alignment and are well packed to form a uniform carpet-style forest with a thickness of 150 μm. High magnification image is also given in Fig. 2b, showing that most of carbon nanotubes are quite straight and parallel to each other. The interspaces between individual CNTs are less than hundreds of nanometers. The HRTEM image of typical CNTs is shown in Fig. 2c. The CNTs have an average inner-diameter of around 8 nm and each CNT consists of 15–30 layers of concentric graphene sheets with layer distance of ∼0.34 nm. Most of the tubes are quite straight and continuously hollow, but some bamboo structures and bridged tube walls can also be observed.

The morphology of the HKUST-1 can be seen in Fig. 2d, the pristine samples display an octahedral shape with sharp edges and the original particle size is around 50 microns. Fig. 2e and f shows the CNTs become tortuous, and the HKUST-1 crystals are grown along the external surface of CNTs, filling up the gaps between CNTs after the confined growth of HKUST-1 into VACNT carpet. The morphology of HKUST-1 is also altered significantly by growing in the confined interspace of VACNT. It is noteworthy that the crystal size of HKUST-1 in the confinement growth is much smaller (sub-micron) than that of the free grown HKUST-1 (Fig. 2d). Similar findings have been reported that nano-sized HKUST-1 crystals have been synthesized in the confinement growth of HKUST-1 inside anodic aluminum oxide.[31] Closer examination of the cross-section of HKUST-1/VACNT composite reveals that higher density of HKUST-1 is found on the exposed side of VACNT, while lower crystals density on the substrate side. The difference in the crystal growth density might be attributed to the diffusion resistance of HKUST-1 precursor in VACNT arrays. Different morphology was observed in HKUST-1/VACNT composite if untreated VACNTs were applied for HKUST-1 confined growth (Fig. S2, ESI†). Severe space occlusion was seen, and the large HKUST-1 particles can only be observed on the tips of VACNT arrays. While in the interspaces of VACNTs, there hardly exist HKUST-1 crystals. Compared to the better dispersion of HKUST-1 inside the treated VACNT arrays, it can be concluded that the pre-treatment of the VACNTs can facilitate the HKUST-1 growth; the surface functional groups on CNTs can act as nucleation sites and form MOFs by heterogeneous nucleation.[32–34]

Fig. 1 (a) XRD spectra of the HKUST-1 (black dots: observed, red line: simulated) and HKUST-1/VACNTs; (b) the structure diagram of HKUST-1 (red: O, blue: Cu, black: C, green: H).

The thermal stability of derived HKUST-1, VACNTs and HKUST-1/VACNT hybrid were investigated by TGA, as shown in Fig. S3 (ESI†). The initial temperature of weight loss in VACNT was observed until ~550 °C, indicating the high graphitic degree of the as-synthesized VACNT arrays. The oxidation ends above 650 °C and the burnt residue can be assigned to the iron oxide catalyst residue in the VACNTs. As to HKUST-1, a steady weight loss up to the temperature of 320 °C is resulted from the removal of intra crystalline DMF. The steady weight loss indicates a slow release of DMF. Compared to HKUST-1, the solvent removal in HKUST-1/VACNT hybrid finishes at lower temperature (~300 °C). The easy solvent removal in hybrid can be attributed to the confinement growth of small HKUST-1 particles and the formation of effective solvent diffusion paths in the hierarchical porous structure.

The dramatic weight loss in HKUST-1 and HKUST-1/VACNT at beyond 350 °C is due to the decomposition of trimesic acid linkers, leaving CuO as the final product.[28] For the HKUST-1/VACNT composite, the decomposition of trimesic acid linkers above 350 °C leads to the release of oxygen atom and the exposure of Cu metal, which may involve the catalytic oxidation of VACNTs and destroy their graphitic structure. In this case, the decomposition of VACNTs started at lower temperature and completed before reaching 650 °C. The residues are the mixture of copper oxide and iron oxide from HKUST-1 and VACNTs, respectively. For the evaluation of the HKUST-1 contents in the composite, the weight loss from linker decomposition in HKUST-1 and HKUST-1/VACNT was calculated. The initial decomposition temperature (Ti) was 305 and 290 °C for HKUST-1 and HKUST-1/VACNT composite, respectively. The residue weight reached to a steady platform at ~350 °C, which is the terminal decomposition temperature. Since the VACNTs are stable at this temperature range (290/305 °C to 350 °C), the ratio of the weight loss percentage between HKUST-1/VACNT and HKUST-1 reflects the HKUST-1 content in the composite. The weight ratio of HKUST-1 (θ) in the HKUST-1/VACNT composite is calculated as:

$$\theta = \frac{m_{\text{i-composite}} - m_{\text{t-composite}}/m_{\text{i-composite}}}{m_{\text{i-HKUST}} - m_{\text{t-HKUST}}/m_{\text{i-HKUST}}} \times 100\% \quad (1)$$

where $m_{\text{i-HKUST}}$ and $m_{\text{i-composite}}$ are the sample weights of HKUST-1 and HKUST-1/VACNT composite at the initial decomposition temperature, $m_{\text{t-HKUST}}$ and $m_{\text{t-composite}}$ are the sample weights of HKUST-1 and HKUST-1/VACNT composite at the terminal decomposition temperature, respectively. The HKUST-1 content in composite is therefore calculated to be around 43 wt%. To further confirm the HKUST-1 content, the elemental analysis on HKUST-1/VACNT composite was conducted by EDS (Fig. S4 and Table S2, ESI†). Based on the mole ratio of copper and carbon, the HKUST-1 content in the HKUST-1/VACNT composite was calculated as 46.5 wt%, similar to the result derived from weight loss. In addition, the HKUST-1 loading percentage can be affected by the areal density and height of VACNTs which are fluctuated during the CVD growth. In this study, the variation of HKUST-1 loading content on different batches of VACNTs was less than 10%.

Nitrogen sorption experiments were performed on HKUST-1, as-synthesized VACNTs and HKUST-1/VACNT composite. The isotherms and cumulative pore volume results were shown in Fig. S5 (ESI†). The multipoint BET surface area and pore volume were calculated and listed in Table 1. In order to compare the properties of synthesized HKUST-1/VACNT composite, the hypothetical values were also calculated based on mixing the HKUST-1 and VACNT at same weight ratio as in the synthesized HKUST-1/VACNT composite. HKUST-1 exhibits high amount of nitrogen sorption at low pressure and its isotherm is type I, typical for microporous materials. The hysteresis indicates the delayed desorption potentially caused by the hindrance in N_2 removal due to the presence of solvent residue molecules. The BET surface area of the derived HKUST-1 is 1382.6 m² g⁻¹, in line with previous reported values (1270 m² g⁻¹ (ref. 35) and 1333 m² g⁻¹ (ref. 36)). VACNT arrays exhibit a type IV isotherm based on IUPAC classification,[37] suggesting the existence of mesopores in the samples. Its BET surface area is 53.9 m² g⁻¹, including the outer and the interspaced surface area of the arrays, as well as a few of interior sites of open-ended CNTs.

HKUST-1/VACNT composite exhibits a Type II isotherm, indicating the presence of both mesopores and micropores. The composite shows a significantly higher BET surface area (726.7 m² g⁻¹) than pure VACNTs (53.9 m² g⁻¹). The excess N_2 adsorption is attributed to both surface area and pore volume raise from inter-grown HKUST-1. For comparison, the VACNT was physically mixed with same content of HKUST-1 (43%), and the N_2-adsorption isotherm of the mixture is shown in the Fig. S6 (ESI†). The surface area of the physical-mixed HKUST-1-VACNTs is measured to be consistent with the calculated hypothetical value shown in Table 1. Moreover, its surface area was significantly lower (630.3 m² g⁻¹) that that of the synthesized HKUST-1/VACNT hybrid. For pore volume, it is obvious that the synthesized HKUST-1/VACNT composite exhibits much higher porosity than the hypothetical physical mixture of VACNT and HKUST-1, especially in the mesopore range. The enhanced surface area and porosity from the confinement growth of HKUST-1 inside VACNT arrays indicates that synergistic interaction between HKUST-1 and VACNT. The functional groups on CNTs provide heterogeneous nucleation sites for the growth of small HKUST-1 crystals along the CNTs, resulting in the mesoporous and microporous volume increment of the final HKUST-1/VACNT hybrid.

As shown in Fig. S5b (ESI†), VACNTs present almost no cumulative pore volume in the micropore range, since the diameter of CNTs is in the mesopore range and most of tubes are close-ended. On the contrary, HKUST-1 is dominated by micropores; the dramatic cumulative pore volume increment occurs mainly in micropore range while negligible in mesoporous range. The small mesoporous volume can be assigned to the aggregation pores. Compared to pure HKUST-1, the total micropore volume of HKUST-1/VACNT composite reduces due to the component of low-microporous VACNT (Table 1). It is also noteworthy that a sharp increase of accumulated pore volume exists in the micropore range, owing to the additional micropores formed between HKUST-1 and CNTs. Also the mesoporous volume of synthesized composite is three times

Table 1 Parameters of the porous structures of HKUST-1, VACNT and HKUST-1/VACNT composite

	BET surface area ($m^2\ g^{-1}$)	Total volume ($cm^3\ g^{-1}$)	Mesopore volume ($cm^3\ g^{-1}$)	Micropore volume ($cm^3\ g^{-1}$)
VACNT	53.9	0.066	0.041	0.025
HKUST-1	1382.6	0.649	0.078	0.571
HKUST-1/VACNT composite	726.7	0.466	0.174	0.292
HKUST-1/VACNT mixture[a]	625.2	0.317	0.057	0.260

[a] Hypothetical values derived assuming the physical mixture of the VACNT and HKUST-1.

higher than that of hypothetical mixture. The significant mesopore volume increase indicates the formation of hierarchical porous morphology by the *in situ* growth of HKUST-1 into VACNT arrays. Different types of functional groups on VACNT will lead to HKUST-1 grown with relatively disordered structure. The increment of the porosity can be assigned to this disordered arrangement in composite structure.[13]

As reported in the previous reference, HKUST-1 demonstrated the potential of CO_2/N_2 separation in the post- and precombustion capture technologies.[36] In this study, the adsorption capacities of pure CO_2 and N_2 for HKUST-1/VACNT composite were evaluated and shown in Fig. 3, in comparison to HKUST-1 and physical mixture of the HKUST-1/VACNT (Fig. S7, ESI†). All gas adsorption is completely reversible. The CO_2 uptake on both samples shows a gradual increase with pressure, and the increment slope of CO_2 is much higher than that of N_2, indicating a disproportionately high affinity and adsorption capacity for CO_2 on both samples. The high adsorption capacity of CO_2 is mostly attributed to the specific interactions between quadrupolar CO_2 molecules and partial positive charges on the coordinatively unsaturated metal sites in HKUST-1.[38] At 0 °C and 132 kPa, the CO_2 adsorption capacities on HKUST-1, the HKUST-1/VACNT composite and the physical mixture of VACNTs and HKUST-1 are 9.5, 3.5 and 3.1 mmol g^{-1}, respectively. The adsorption capacities of pure CO_2 on the HKUST-1/VACNT composite are higher than that on the physical mixture of VACNTs and HKUST-1, which can be assigned to the synergistic effect between HKUST-1 and VACNT *via* the confinement growth of HKUST-1. On the other hand, the adsorption capacity is exothermic as shown by the decrease of the equilibrium capacity at higher temperature. The CO_2 adsorption value on

the physical mixture of HKUST-1 and VACNTs is also calculated and compared with the measured high-pressure CO_2 adsorption value on HKUST-1/VACNT composite (Fig. S8, ESI†). The higher CO_2 adsorption of the composite over the hypothetical mixture value shows the synergistic effect between HKUST-1 and VACNT, probably derived from the increase in the hypothetical surface area and porosity (Table 1). Also the enhancement of sorption capacity can be attributed to the reducing of HKUST-1 crystal size.[39]

The measured CO_2 and N_2 sorption data can be well fitted by the Langmuir–Freundlich model (Fig. S9, ESI†), with the derived parameters shown in Table S3 (ESI†). The calculated saturation capacities of CO_2 and N_2 on the HKUST-1 are 14.12 and 4.62 mmol g^{-1}, respectively. On contrary, the HKUST-1/VACNT hybrid can absorb 7.83 and 2.04 mmol g^{-1} of CO_2 and N_2 at saturation. Considering the weight percentage of HKUST-1 in the composite, the normalized CO_2 adsorption capacity per gram of HKUST-1 in the hybrid can reach to a value significantly larger than that of the pure HKUST-1, 17.65 mmol $g_{HKUST-1}^{-1}$, while the normalized N_2 adsorption capacity (4.6 mmol $g_{HKUST-1}^{-1}$) is similar to that of the HKUST-1. Therefore, the improvement on CO_2/N_2 adsorption selectivity can be expected in the composite, as shown in Fig. 4. The selectivity shows a descending trend with the operation pressure. In the whole pressure range, the gas adsorption is more selective on HKUST-1/VACNT hybrid than that on pure HKUST-1, which can be attributed to the cooperative interaction between HKUST-1 and VACNTs.

The curvature of planar graphene layers into cylinders in CNTs induces the electron transfer from the concave inner
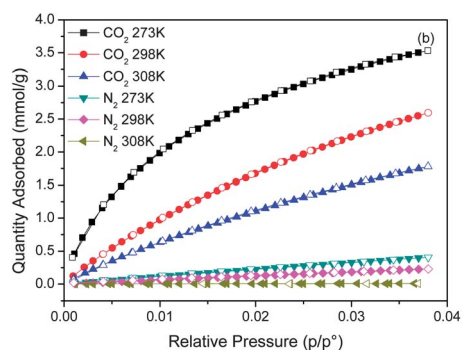
Fig. 3 CO_2 and N_2 adsorption isotherms of HKUST-1/VACNT composite at different temperatures.
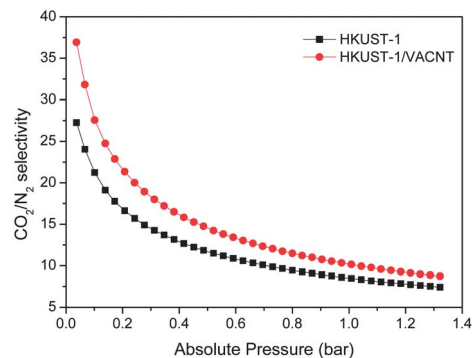
Fig. 4 The CO_2/N_2 adsorption selectivity on HKUST-1 and HKUST-1/VACNT composite.

surface to the convex outer surface of CNTs, leading to higher electron density on the CNT external surface than inside CNT channels. In this case, by growing HKUST-1 on the CNT external surface, the electrostatic interactions of CO_2 adsorption may be enhanced. The strength of electrostatic interactions can influence the gas separation especially for the gas components with different dipoles/quadrupoles.[40] Therefore, the enhanced CO_2/N_2 selectivity can be observed as in Fig. 4.

To better understand the adsorption difference between HKUST-1 and HKUST-1/VACNT hybrid, the Clausius–Clapeyron equation (eqn (2)) was used to calculate the isosteric heats of adsorption, ΔH_{ads}, from the slope of the best-fit line for $\ln p$ versus T^{-1} at each loading.

$$(\ln p)_q = \left(\frac{\Delta H_{ads}}{R}\right)\left(\frac{1}{T}\right) + C \tag{2}$$

here, q is the amount of adsorbed gas (mmol g^{-1}) at 273 K, 298 K and 308 K, p is the exact pressure (bar), T is the absolute temperature (K), R is the ideal gas constant (J mol^{-1} K^{-1}).

As shown in Fig. 5, the isosteric heat of CO_2 adsorption on HKUST-1 maintains at around 29 kJ mol^{-1}, which is in line with the reported values for HKUST-1 framework (29.8 kJ mol (ref. 41) and 28.0 kJ mol^{-1} (ref. 18)). In contrast, the isosteric heat of CO_2 adsorption on HKUST-1/VACNT hybrids shows a descending trend with increasing CO_2 adsorption amount; the calculated heat for the composite is 37.0 kJ mol^{-1} at low adsorption amount, much higher than that for HKUST-1. This trend matches well with the findings in HKUST-1/AAO composite.[31] Therefore, it is clear that the hierarchical structure of HKUST-1/VACNT hybrid can facilitate the CO_2 storage at low pressure. On the other hand, the isosteric heat of N_2 adsorption on HKUST-1/VACNT hybrid displays similar trends as that of HKUST-1, yet with the lower values. The variation of adsorption heat on CO_2 and N_2 with different dipoles/quadrupoles can be attributed to the change of electrostatic interaction by CNTs. It can be seen that by the confined growth of HKUST-1 in VACNT arrays, stronger affinity of CO_2 but weaker affinity of N_2 molecules is resulted for the composite, thus enhancing the adsorption selectivity (Fig. 4). However, lower gas saturation capacity for HKUST-1/VACNT is observed than HKUST-1. One feasible way to further enhance the saturation capacity of HKUST-1/VACNT hybrid is to increase the HKUST-1 content in the composite *via* the modification of synthesis conditions.
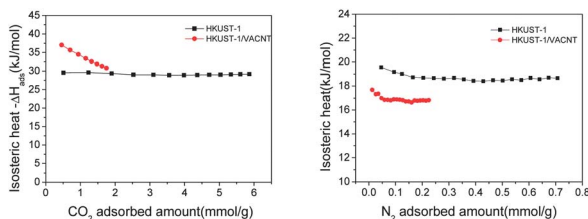
Fig. 5 The isosteric heats of adsorption ($-\Delta H_{ads}$) on the HKUST-1 and HKUST-1/VACNT composite.

Conclusions

In summary, the novel carbon/MOF composite material has been synthesized by growing HKUST-1 into the interspace of the VACNT arrays. The interspaces of VACNT arrays provide the space for the confined growth and result in the derived sub-micron HKUST-1 crystals. Compared to pure VACNT, the mesopore and micropore volumes of HKUST-1/VACNT hybrid are significantly improved. The CO_2 and N_2 adsorption was evaluated on this HKUST-1/VACNT composite. The saturation capacities of CO_2 on HKUST-1/VACNT hybrid can reach to 7.83 mmol g^{-1} at 298 K. Compared to HKUST-1, the adsorption selectivity of CO_2 over N_2 on HKUST-1/VACNT hybrids is enhanced in all the pressure range, owing to the synergistic effect between HKUST-1 and VACNTs. The HKUST-1/VACNT hybrids show some promising prospects, including the high adsorption capacity, the tunable porosity, and the bulk shape. Further work can be conducted on thicker VACNT arrays to synthesize larger MOF/VACNT bulk composites. The areal density of VACNTs can also be adjusted by CVD synthesis and post-functionalisations for the controllable MOFs growth. The approach developed in the study could also propose a way for the use of VACNTs to develop hierarchically porous structured materials for the applications that require favourable mass transport, such as catalysis, gas separation, energy storage and conversion.

Acknowledgements

Notes and references

1 H. Li, M. Eddaoudi, M. O'Keeffe and O. M. Yaghi, *Nature*, 1999, **402**, 276–279.

2 Z. Ni, J. P. Jerrell, K. R. Cadwallader and R. I. Masel, *Anal. Chem.*, 2007, **79**, 1290–1293.

3 Z. R. Herm, J. A. Swisher, B. Smit, R. Krishna and J. R. Long, *J. Am. Chem. Soc.*, 2011, **133**, 5664–5667.

4 J. Lee, O. K. Farha, J. Roberts, K. A. Scheidt, S. T. Nguyen and J. T. Hupp, *Chem. Soc. Rev.*, 2009, **38**, 1450–1459.

5 P. Horcajada, C. Serre, G. Maurin, N. A. Ramsahye, F. Balas, M. Vallet-Regi, M. Sebban, F. Taulelle and G. Ferey, *J. Am. Chem. Soc.*, 2008, **130**, 6774–6780.

6 G. Lu and J. T. Hupp, *J. Am. Chem. Soc.*, 2010, **132**, 7832–7833.

7 H. Bux, F. Liang, Y. Li, J. Cravillon, M. Wiebcke and J. Caro, *J. Am. Chem. Soc.*, 2009, **131**, 16000–16001.

8 H. Guo, G. Zhu, I. J. Hewitt and S. Qiu, *J. Am. Chem. Soc.*, 2009, **131**, 1646–1647.

9 A. U. Czaja, N. Trukhan and U. Muller, *Chem. Soc. Rev.*, 2009, **38**, 1284–1293.

10 F. Rezaei, A. Mosca, P. Webley, J. Hedlund and P. Xiao, *Ind. Eng. Chem. Res.*, 2010, **49**, 4832–4841.

11 X. S. Wang, S. Ma, D. Sun, S. Parkin and H. C. Zhou, *J. Am. Chem. Soc.*, 2006, **128**, 16474–16475.

12 L. G. Qiu, T. Xu, Z.-Q. Li, W. Wang, Y. Wu, X. Jiang, X. Y. Tian and L.-D. Zhang, *Angew. Chem., Int. Ed.*, 2008, **47**, 9487–9491.

13 C. Petit, J. Burress and T. J. Bandosz, *Carbon*, 2011, **49**, 563–572.

14 S. J. Yang, J. Y. Choi, H. K. Chae, J. H. Cho, K. S. Nahm and C. R. Park, *Chem. Mater.*, 2009, **21**, 1893–1897.

15 A. M. B. Furtado, J. Liu, Y. Wang and M. D. LeVan, *J. Mater. Chem.*, 2011, **21**, 6698–6706.

16 J. Gorka, P. F. Fulvio, S. Pikus and M. Jaroniec, *Chem. Commun.*, 2010, **46**, 6798–6800.

17 Z. Xiang, X. Peng, X. Cheng, X. Li and D. Cao, *J. Phys. Chem. C*, 2011, **115**, 19864–19871.

18 Z. Xiang, Z. Hu, D. Cao, W. Yang, J. Lu, B. Han and W. Wang, *Angew. Chem., Int. Ed.*, 2011, **50**, 491–494.

19 K. P. Prasanth, P. Rallapalli, M. C. Raj, H. C. Bajaj and R. V. Jasra, *Int. J. Hydrogen Energy*, 2011, **36**, 7594–7601.

20 M. Anbia and V. Hoseini, *Chem. Eng. J.*, 2012, **191**, 326–330.

21 C. Petit and T. J. Bandosz, *Adv. Mater.*, 2009, **21**, 4753–4757.

22 C. Petit and T. J. Bandosz, *Adv. Funct. Mater.*, 2010, **20**, 111–118.

23 C. Petit, L. Huang, J. Jagiello, J. Kenvin, K. E. Gubbins and T. J. Bandosz, *Langmuir*, 2011, **27**, 13043–13051.

24 C. Petit, B. Mendoza and T. J. Bandosz, *ChemPhysChem*, 2010, **11**, 3678–3684.

25 B. Levasseur, C. Petit and T. J. Bandosz, *ACS Appl. Mater. Interfaces*, 2010, **2**, 3606–3613.

26 M. Kumar and Y. Ando, *Chem. Phys. Lett.*, 2003, **374**, 521–526.

27 L. Ge, L. Wang, A. Du, M. Hou, V. Rudolph and Z. Zhu, *RSC Adv.*, 2012, **2**, 5329–5336.

28 J. Liu, J. T. Culp, S. Natesakhawat, B. C. Bockrath, B. Zande, S. G. Sankar, G. Garberoglio and J. K. Johnson, *J. Phys. Chem. C*, 2007, **111**, 9305–9313.

29 S. S.-Y. Chui, S. M.-F. Lo, J. P. H. Charmant, A. G. Orpen and I. D. Williams, *Science*, 1999, **283**, 1148–1150.

30 M. Hartmann, S. Kunz, D. Himsl, O. Tangermann, S. Ernst and A. Wagener, *Langmuir*, 2008, **24**, 8634–8642.

31 M. Maksoud, N. Roques, S. Brandes, L. Arurault and J.-P. Sutter, *J. Mater. Chem. A*, 2013, **1**, 3688–3693.

32 S. Hermes, F. Schröder, R. Chelmowski, C. Wöll and R. A. Fischer, *J. Am. Chem. Soc.*, 2005, **127**, 13744–13745.

33 M. Shoaee, M. W. Anderson and M. P. Attfield, *Angew. Chem., Int. Ed.*, 2008, **47**, 8525–8528.

34 C. Scherb, A. Schödel and T. Bein, *Angew. Chem., Int. Ed.*, 2008, **47**, 5777–5779.

35 J. Moellmer, A. Moeller, F. Dreisbach, R. Glaeser and R. Staudt, *Microporous Mesoporous Mater.*, 2011, **138**, 140–148.

36 Q. Min Wang, D. Shen, M. Bulow, M. Ling Lau, S. Deng, F. R. Fitch, N. O. Lemcoff and J. Semanscin, *Microporous Mesoporous Mater.*, 2002, **55**, 217–230.

37 R. Pierotti and J. Rouquerol, *Pure Appl. Chem.*, 1985, **57**, 603–619.

38 K. Sumida, D. L. Rogow, J. A. Mason, T. M. McDonald, E. D. Bloch, Z. R. Herm, T.-H. Bae and J. R. Long, *Chem. Rev.*, 2012, **112**, 724–781.

39 L. Ge, W. Zhou, V. Rudolph and Z. Zhu, *J. Mater. Chem. A*, 2013, **1**, 6350–6358.

40 J.-R. Li, Y. Ma, M. C. McCarthy, J. Sculley, J. Yu, H.-K. Jeong, P. B. Balbuena and H.-C. Zhou, *Coord. Chem. Rev.*, 2011, **255**, 1791–1823.

41 C. R. Wade and M. Dinca, *Dalton Trans.*, 2012, **41**, 7931–7938.